Uncovering the role of unsaturated coordination defects in manganese oxides for concentrated solar-heating photothermal OVOCs oxidation: Experimental and DFT explorations

Shengpeng Mo [a], Xin Zhao [a], Lili Huang [a], Jiangjing Zhou [a], Shuangde Li [b,*], Ruosi Peng [d], Zhihong Tu [a], Lei Liao [a], Qinglin Xie [a], Yunfa Chen [b], Yanan Zhang [a,*], Daiqi Ye [c]

[a] College of Environment Science and Engineering, Guilin University of Technology, Guilin 541004, PR China
[b] State Key Laboratory of Multi–phase Complex Systems, Institute of Process Engineering, Chinese Academy of Sciences, Beijing 100190, PR China
[c] School of Environment and Energy, South China University of Technology, Guangzhou 510006, PR China
[d] School of Environment and Civil Engineering, Dongguan University of Technology, Dongguan 523808, PR China

ARTICLE INFO

ABSTRACT

In this study, we innovatively develop a concentrated photothermal catalysis (CPTC) system with a cost-effective solar concentrator to efficaciously achieve light-to-heat conversion, and combine a defect engineering strategy to design Mn_3O_4-based catalysts with unsaturated coordination defects (O and Mn atoms) for solar-heating photothermal ethyl acetate oxidation without additional artificial-energy input. As a result, Mn_3O_4-3 exhibits outstanding photothermal catalytic performance for ethyl acetate and other OVOCs oxidation under weak simulated sunlight even natural sunlight irradiation. The enriched unsaturated defects in Mn_3O_4-3 with lower Mn-O and Mn-Mn coordination numbers not only improve the concentration of surface reactive species (Mn^{4+} and O_{ads}), but also regulate the energy-band structure to further promote the light absorption capacity and charge separation. Experimental and theoretical evidences demonstrate that the generation of abundant Mn defects is conducive to the ethyl acetate dissociation/hydrolysis into key intermediates, while the existence of more O vacancies synergistically facilitates the O_2 dissociation toward highly reactive O* participating in the deep oxidation of key intermediates. Moreover, in-situ DRIFTS and DFT results reveal the reaction pathway expansion (Pathway I and II) of photothermal ethyl acetate oxidation on manganese oxides under sunlight irradiation. This work provides an attractive CPTC technology for VOCs removal in energy and environmental application.

1. Introduction

Oxygenated volatile organic compounds (OVOCs) as one of typical VOC pollutants, such as ethyl acetate, acetone, methanol and so on, are main precursors for the formation of $PM_{2.5}$, ozone and photochemical smog [1,2]. At present, thermal catalytic oxidation (TCO) is recognized as one of the most promising technologies for VOCs degradation in industrial application, but suffers from the energy consumption and removal efficiency problems [1,3–6]. To solve the above problems, an effective strategy of photothermal catalytic oxidation (PTCO) has been developed to eliminate VOCs via utilizing inexhaustible solar energy, which combines the advantages of both thermocatalysis and photocatalysis [2,5,7–9]. For instance, Deng et al. [5] prepared MOF-derived mesoporous disk-like 0.26 Pd/3.2 N-TiO$_2$ catalyst for photothermal catalytic oxidation of ethyl acetate under light irradiation condition (300 mW cm^{-2}). The improvement of photothermal catalytic performance of 0.26 Pd/3.2 N-TiO$_2$ is attributed to the result of photothermal synergy including the enhanced light absorption capacity and the promoted charge separation. Our group also designed a series of Co-MOF-74-derived Co_3O_4-based materials for photothermal catalytic ethyl acetate oxidation under visible-IR light intensity of 480 mW cm^{-2} [7]. The as-prepared Co_3O_4-M-3 catalyst exhibited the greatest photothermal catalytic performance for ethyl acetate oxidation (about 92 %), and its suitable energy band level and Z-scheme charge transfer pathway effectively facilitated the visible-light absorption capacity, the transfer and separation of photogenerated charge carriers. Certainly, the

* Corresponding authors.
E-mail addresses: sdli@ipe.ac.cn (S. Li), zyanan@glut.edu.cn (Y. Zhang).

light-driven photothermal catalytic efficiencies for VOCs are affected by light absorption capacity, charge separation and active sites.

In recent years, various defect engineering strategies have been developed to improve the light absorption capacity, charge separation and active sites of catalysts [10–12]. Simultaneously, the formation of defects in catalysts could also effectively adjust the physical and chemical properties [8,10,11,13]. For example, Li et al. [10] reported that a δ-MnO$_2$ treated with urea-H$_2$O$_2$ defect engineering exhibited more excellent thermal and photothermal activities of propane oxidation compared to reducing etchants urea and vitamin C. Urea-H$_2$O$_2$ treatment provided high concentration of Mn^{4+} and surface-active oxygen species, and produced abundant oxygen vacancies to improve the charge separation. Zhao et al. [11] proposed a solvent-induced reduction strategy to design Cu/Mn-based catalysts with interfacial oxygen vacancies for enhanced light-driven photothermal catalytic toluene degradation (126 mW cm^{-2}). The optimal M-Cu/MnO$_x$ nanosheets displayed excellent light absorptivity and photogenerated carrier separation efficiency. Although significant progress has been achieved in the defect engineering development of manganese-based oxides, the relevant mechanism theories of defects are still remains in the stage of superficial experimental data and lack in-depth theoretical research, especially cation defects [13,14]. Moreover, the intense artificial light (100–700 mW cm^{-2}) in most published researches must be provided to drive the global temperature of catalysts for photothermal catalytic VOCs elimination, which is much higher than the irradiation intensity of outdoor natural sunlight (less than 100 mW cm^{-2}) due to restricted solar energy utilization [15]. Thus, one is that experimental and theoretical calculations need to be combined to further understand the reaction mechanism at the atomic levels. On the other hand, it is highly anticipated that developing a new concentrated photothermal catalysis (CPTC) system achieves the utmost harmonic utilization of natural sunlight to meet the operating temperature for VOCs oxidation via constructing a light concentration device.

Based on the above-mentioned considerations, we synthesized a series of defective Mn$_3$O$_4$-based catalysts with oxygen vacancy (V$_O$) and Mn defect/vacancy (V$_{Mn}$) via solvent- and template-induced Mn-BTC isomers as sacrificial templates. Defective Mn$_3$O$_4$-based catalysts were further evaluated for concentrated solar-heating photothermal ethyl acetate oxidation via a plastic Fresnel lens to focus simulated full-spectrum sunlight (AM 1.5 G filter, 27.7 mW cm^{-2}). Impressively, the optimal Mn$_3$O$_4$-3 with abundant unsaturated defects (O and Mn) displayed efficient and steady solar-heating photothermal ethyl acetate oxidation (about 97 % conversion) under weak simulated sunlight irradiation even natural sunlight. Meanwhile, the dominant role of unsaturated coordination defects and the catalytic mechanism of photothermal ethyl acetate oxidation were deeply revealed by experimental characterizations and density functional theory (DFT) calculations. This work could be conducive to in the development of high-efficiency photothermal catalysts and maximized solar energy utilization for VOCs oxidation.

2. Experimental section

2.1. Preparation of Mn$_3$O$_4$-x photocatalysts :

Mn$_3$O$_4$-x compounds were synthesized by pyrolysis of Mn-BTC precursors. Typically, 15 mmol 1, 3, 5-trimesic acid (H$_3$BTC) and 5 mmol Mn(CH$_3$COO)$_2$•4 H$_2$O were dissolved in 150 mL absolute ethanol and 50 mL deionized water to form A and B solutions, respectively. Then, the above two solutions were rapidly mixed under magnetic stirring. After magnetic stirring for 15 h at room temperature, the resulting product was filtered and washed with ethanol and deionized water for several times, and followed by drying to obtain a Mn-BTC-x precursor. Finally, the Mn-BTC-x precursor was placed in a tube furnace and heated from room temperature to 400 °C with a heating rate of 2 °C min^{-1} in air atmosphere for 3 h. After cooling to room temperature, the black/brown

Mn$_3$O$_4$-x product (x represented the volume ratio of used ethanol/water in the synthesis process, x = 3, 2 and 1) was obtained.

2.2. Preparation of Mn$_3$O$_4$-P-x photocatalysts :

Mn-BTC-P-x precursors and Mn$_3$O$_4$-P-x compounds were also synthesized according to the above method with minor modification. The difference was the addition of 2.0 g polyvinyl pyrrolidone (PVP K29–32, MW~58000) to Mn(CH$_3$COO)$_2$•4 H$_2$O solution in the synthesis process. After calcination at 400 °C for 3 h, the black/brown Mn$_3$O$_4$-P-x product (P represented the used PVP in the synthesis process) was obtained.

3. Results and discussion

3.1. Crystal structure and morphology characterization

A series of Mn-BTCs were prepared by optimizing two (surfactant and solvent) conditions, and the products were marked as Mn-BTC-x and Mn-BTC-P-x, respectively. As shown in Fig. S1, the X-ray diffraction (XRD) patterns of Mn-BTC-x and Mn-BTC-P-x are well matched with the reported literatures (CCDC #810694) [16–18]. Interestingly, as the ethanol/water solvent ratio was varied from 3 to 1, the obtained Mn-BTC-1 and Mn-BTC-P-1 distinctly display different crystallographic structure, implying that controlling preparation solvent effectively induces the structural isomerism of Mn-BTC. Similar MOF isomer phenomena have also been reported in the previous study [19]. As displayed in Fig. 1, the Mn-BTC-x and Mn-BTC-P-x exhibit a series of beautiful and biomimetic morphologies. In terms of solvent-induced Mn-BTC-x without PVP (Fig. 1a-f), the Mn-BTC-3 with high ethanol/water ratio presents an urchin-like microsphere assembled by a lot of nanorods about 100–200 nm in diameter, and the Mn-BTC-2 and Mn-BTC-1 appear a polygonal nanocolumn with a diameter of approximately 3–4 μm and dandelion microsphere with self-assembly numerous nanowires, respectively. For template-induced Mn-BTC-P-x with the addition of 2.0 g PVP (Fig. 1g-l), the Mn-BTC-P-3, Mn-BTC-P-2 and Mn-BTC-P-1 exhibit a pompon microsphere with a diameter of about 3–5 μm, chrysanthemum microsphere with a diameter of 4 μm and cross-shaped nanobeam with numerous self-assembly tabular nanostrips, respectively. Thus, the above results confirm that the crystal structure and growth orientation of Mn-BTC can be accurately adjusted by template or solvent induction.

After the calcination of above Mn-BTC precursors, these obtained manganese oxides (Mn$_3$O$_4$-x and Mn$_3$O$_4$-P-x) similarly exhibit the main characteristic diffraction peaks of Mn$_3$O$_4$ (JCPDS PDF#80-0382) crystal phase and one weak diffraction peak of Mn$_2$O$_3$ (JCPDS PDF#24-0508) at 2θ of 55.1° (Fig. 2a). In addition, according to the SEM images in Fig. 2b, c and S2, the microscopic morphologies of Mn$_3$O$_4$-x and Mn$_3$O$_4$-P-x are changed on a large scale after the removal of organic ligands and PVP, especially surface subassembly. Mn$_3$O$_4$-3 (Fig. 2b) displays a neuron-like morphology with numerous intersectional branch structures on the surface, in which the branch structures are transformed from the surface self-assembly nanorods of Mn-BTC-3 due to thermal decomposition and structural shrinkage. The polygonal nanocolumn morphology on Mn-BTC-2 is converted into a nanobelt shape with rough surface and visible channels on Mn$_3$O$_4$-2 (Fig. S2a,b), and the dandelion microsphere on Mn-BTC-2 collapses completely into many fine particles on Mn$_3$O$_4$-1 (Fig. S2c,d). Similarly, the Mn$_3$O$_4$-P-3, Mn$_3$O$_4$-P-2 and Mn$_3$O$_4$-P-1 (Fig. 2c and S2e-h) present the surface rough microsphere, rambutan-like shape and nanobeam with self-assembly lots of nanobelts, respectively.

3.2. Catalytic performance for OVOCs oxidation

The solar-heating photothermal performances of all as-prepared Mn$_3$O$_4$-x and Mn$_3$O$_4$-P-x from Mn-BTC isomers, were evaluated in the ethyl acetate oxidation via utilizing a plastic Fresnel lens to concentrate
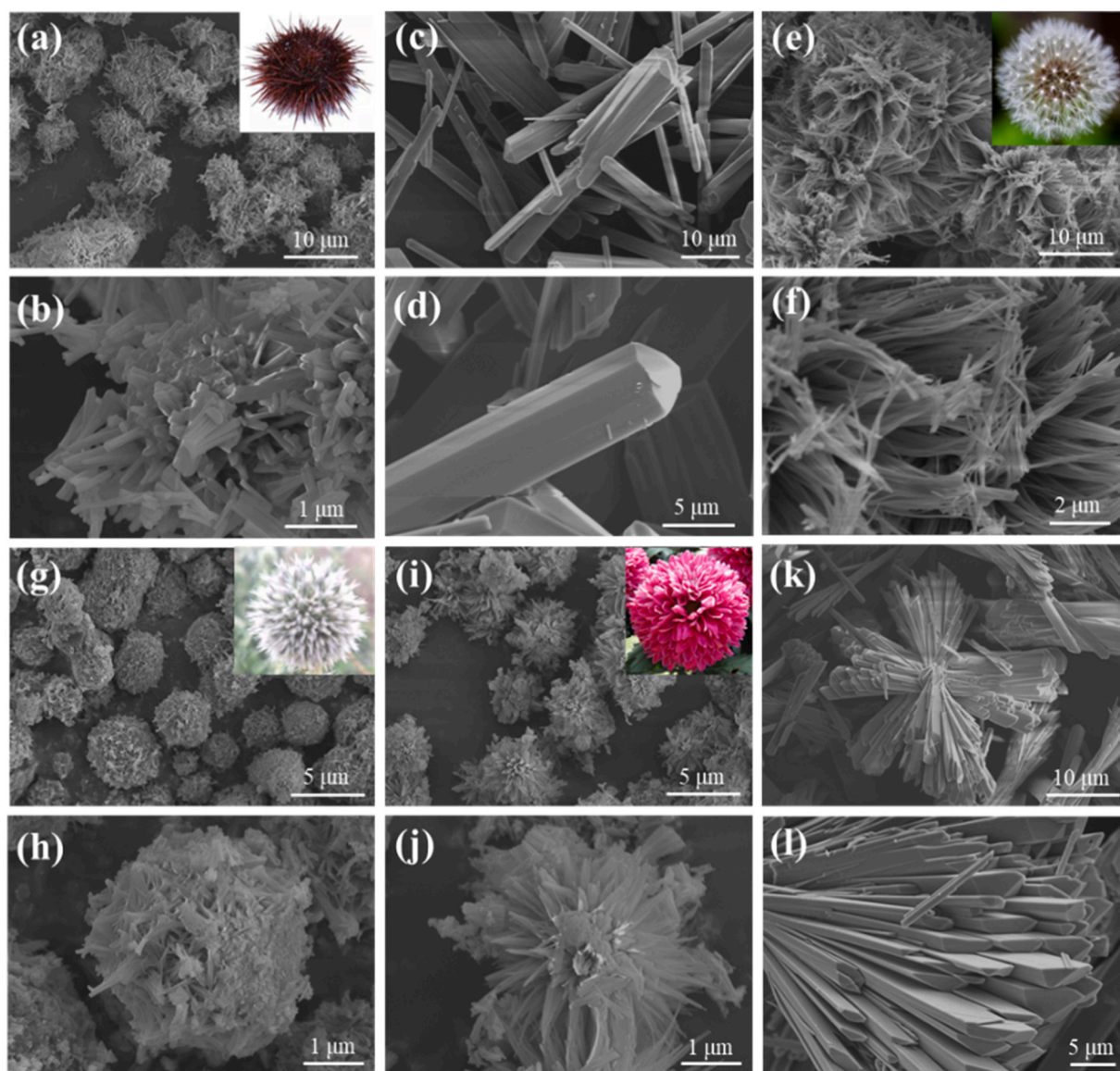
Fig. 1. SEM images of Mn-BTC-x and Mn-BTC-P-x precursors: (a, b) Mn-BTC-3, (c, d) Mn-BTC-2, (e, f) Mn-BTC-1, (g, h) Mn-BTC-P-3, (i, j) Mn-BTC-P-2 and (k, l) Mn-BTC-P-1.

the simulated sunlight irradiation (Xe lamp light intensity of 27.7 mW cm^{-2}). Evidently, Mn_3O_4-3 exhibits the highest catalytic activity (around 97 %) for photothermal ethyl acetate oxidation in Fig. 3a, and the lowest ethyl acetate conversion (about 43 %) is obtained with Mn_3O_4-P-1. Meanwhile, CO_2 yield, by-product (methanol and ethanol, etc) concentration and solar-driven temperature were also monitored in detail. The methanol by-product is detected on all these catalysts, and the methanol concentrations (maximum value 181 ppm) on Mn_3O_4-P-1 are significantly higher than those of other catalysts in Fig. 3b. Besides, low-concentration ethanol by-product is detected on the Mn_3O_4-1 and Mn_3O_4-P-1 catalysts (Fig. S3). The formation of methanol and ethanol by-products is mainly due to the important contribution of ethyl acetate hydrolysis reaction [1], thus the Mn_3O_4-1 and Mn_3O_4-P-1 catalysts with lower ethyl acetate conversion likely produce more higher concentrations of two by-products than other catalysts. As shown in Fig. S4, CO_2 yields on the Mn_3O_4-1 and Mn_3O_4-P-1 catalysts are approximately 10 % lower than its ethyl acetate conversion, and the two indexes of optimal Mn_3O_4-3 catalyst are very close. Fig. 3c shows the solar-driven-heating temperatures over the Mn_3O_4-x and Mn_3O_4-P-x catalysts during the photothermal ethyl acetate oxidation. The stable temperature in

Mn_3O_4-3 is much higher than that of other catalysts, which is further confirmed via the Infrared thermal mappings (Fig. 3d, e). According to the formula $\eta = E_{thermal}/E_{phototons}$ [20,21], the photothermal conversion efficiency (η) of Mn_3O_4-3 and Mn_3O_4-P-1 is indirectly calculated to be 5.3 % and 4.7 % based on the concentrated light intensity of around 720 mW cm^{-2}, respectively (Fig. S5 and S6). It can be found that Mn_3O_4-3 possesses a higher photothermal conversion efficiency than Mn_3O_4-P-1, which may be due to its better absorption ability of sunlight. We also investigated the thermal catalytic behaviors for ethyl acetate oxidation over the Mn_3O_4-3 and Mn_3O_4-P-x catalysts at relevant stable temperature (Fig. S7), and the ethyl acetate conversions, CO_2 yields and methanol by-product concentrations in the photothermal catalysis and thermal catalysis are summarized in Fig. 3f. It is clearly seen that various indexes in photothermal catalysis are effectively improved in comparation with alone thermal catalysis, especially by-product methanol concentration, suggesting the synergetic effect between photocatalysis and thermal catalysis for solar-driven-heating ethyl acetate oxidation.

The influence of WHSV, ethyl acetate concentration and moisture on the ethyl acetate conversion over Mn_3O_4-3 catalyst were also further explored. As displayed in Fig. S8, with the WHSV gradually increases to
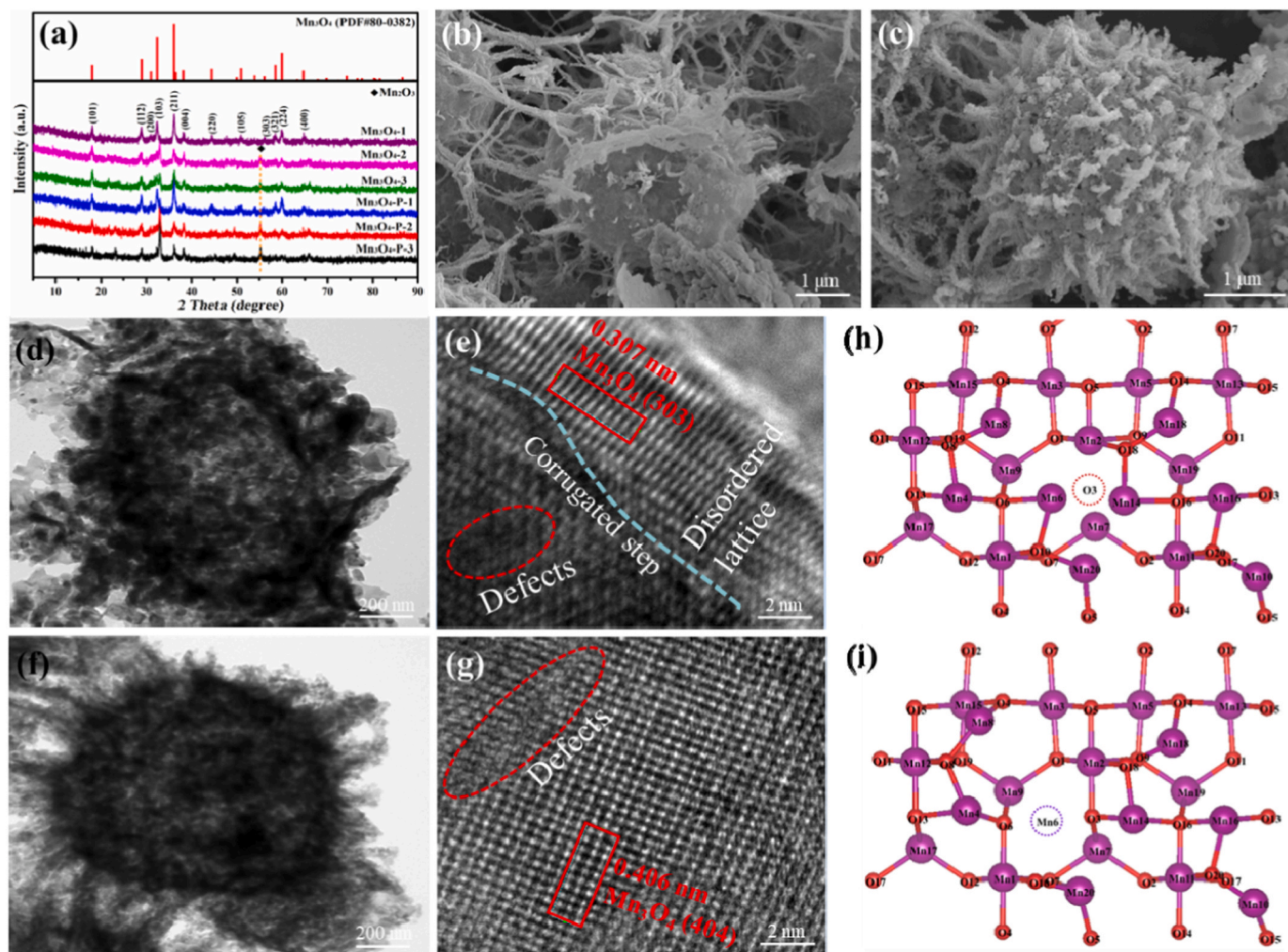
Fig. 2. (a) X-ray diffraction (XRD) patterns of Mn_3O_4-x and Mn_3O_4-P-x catalysts. SEM and TEM images of (b, d and e) Mn_3O_4-3 and (c, f and g) Mn_3O_4-P-2 catalysts, respectively. Optimized (110) surface structure models with (h) oxygen vacancy (V_O) and (i) Mn defect (V_{Mn}) of defective Mn_3O_4.

$60{,}000$ mL g^{-1} h^{-1}, the photothermal ethyl acetate conversion of Mn_3O_4-3 decreases from 97 % to approximately 90 %. Similarly, Mn_3O_4-3 can still maintain high ethyl acetate conversion (around 93 %) at ethyl acetate concentration as high as 2000 ppm (Fig. S9). Water-tolerant test demonstrates that ethyl acetate concentration reduces and remains at about 93 % within 5 vol% moisture (Fig. 3g), indicating that the Mn_3O_4-3 catalyst exhibits desirable moisture resistance. Moreover, The Mn_3O_4-3 catalyst also shows excellent photothermal catalytic performances for other OVOCs (acetone, ethanol and methanol) in Fig. S10. Finally, to verify the feasibility of photothermal catalytic ethyl acetate degradation via using Fresnel lens (Fig. 3h) to concentrate natural sunlight, a simple solar-heating photothermal reaction system (Fig. 3i) was set up outdoor for the experiments. The natural solar flux, solar-heating stable temperature as well as ethyl acetate conversion over Mn_3O_4-3 catalyst on March 14th, 2023, 12:30–15:00 in Guilin (P. R. China) were recorded in Fig. 3j. It is found that the solar-heating temperature can reach up to around 427 °C at noon and gradually decreases to about 280 °C in the afternoon under weak solar irradiation in spring season, and the Mn_3O_4-3 catalyst still maintains 100 % conversion. Outdoor experiments demonstrate that converting natural sunlight to heat/power via a collection equipment will be an energy-saving and environmental strategy for OVOCs degradation without artificial-energy input.

3.3. Analyses of physical and chemical properties

To explore the structural defects and surface chemical compositions, a series of characterization methods were further performed for Mn_3O_4-3 and Mn_3O_4-P-x catalysts. The TEM and HRTEM images (in Fig. S11) observed that the Mn_3O_4-P-3 and Mn_3O_4-P-1 retain the hollow microsphere and nanobelt shape, and its interplanar spacings of about 0.245 and 0.278 nm are ascribed to the (220) and (105) crystal planes of Mn_3O_4, respectively. The Mn_3O_4-3 presents the hollow microsphere with numerous protruding nanosheets/wires on the surface (Fig. 2d), and its lattice fringes with an interplanar spacing of 0.307 nm correspond to the (303) crystal plane of Mn_3O_4. Importantly, it can be observed that there are the phenomena on local dent region, corrugated step and disordered lattice in HRTEM image (Fig. 2e), implying the existence of enriched unsaturated defects in Mn_3O_4-3. Similarly, the lattice-fringe break or local deletion is now also observed in the HRTEM image (Fig. 2g) of Mn_3O_4-P-2, and its morphology well maintains a rambutan-like shape (Fig. 2f) with an interplanar spacing of 0.406 nm corresponding to the (404) crystal plane of Mn_3O_4. XPS results reveal that the Mn/O actual atomic ratios (Table S1) in Mn_3O_4-3 and Mn_3O_4-P-x catalysts are all much lower than the stoichiometric ratio (0.75) of ideal Mn_3O_4, and Mn_3O_4-3 possesses a more lower Mn/O atomic ratio (0.492) than Mn_3O_4-P-x catalysts, indicating the existence of abundant unsaturated defects in Mn_3O_4-3 [14,22]. Optimized (110) surface structure models of ideal and defective Mn_3O_4 are shown in Fig. 2h, I
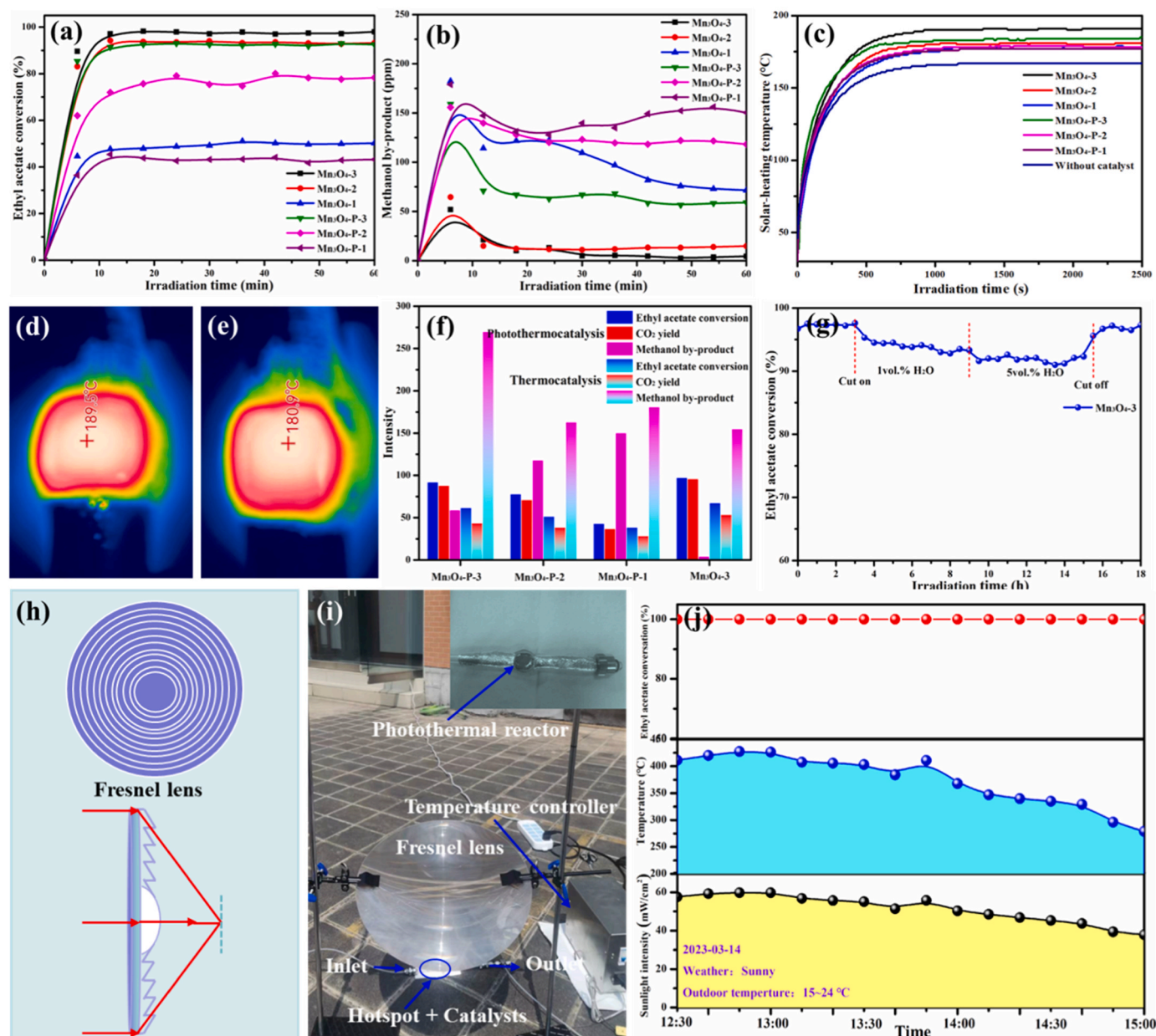
Fig. 3. (a) Ethyl acetate conversion, (b) methanol by-product concentration, (c) solar-driven temperature profiles over the Mn_3O_4-x and Mn_3O_4-P-x catalysts as a function of irradiation time under simulated sunlight irradiation at 27.7 mW cm^{-2}. Solar-driven stable temperature mappings of (d) Mn_3O_4-3 and (e) Mn_3O_4-P-1 obtained via an infrared thermal camera. (f) Catalytic performances in the photothermal catalysis and thermal catalysis. Influence of (g) water-tolerant test for the Mn_3O_4-3 catalyst. (h) Schematic diagram of solar concentrator (plastic Fresnel lens), (i) concentrated solar-heating photothermal system under natural sunlight irradiation concentrated by a Fresnel lens, and (j) solar flux, stable temperature as well as ethyl acetate conversion over the Mn_3O_4-3 catalyst on March 14th, 2023, 12:30–15:00 in Guilin, P. R. China. (Reaction conditions: 100 mL min^{-1} of 1000 ppm ethyl acetate, 0.2 g of catalyst, WHSV = 30,000 mL g^{-1} h^{-1}).

and S12, respectively. According to the Bader charge analyses in Table S2, the neighboring Mn atoms around the O defect site on $Mn_3O_4(110)$-V_O would lose less electrons, while the O atoms nearby the Mn defect site on $Mn_3O_4(110)$-V_{Mn} would gain less electrons compared with those of ideal $Mn_3O_4(110)$. Therefore, the formation of unsaturated defects not only changes the coordination environment of surrounding atoms, but also improves the electronic structure of catalysts for adsorbed and active reactant (O_2/ethyl acetate).

Besides, the Mn 2p, Mn 3s and O 1s XPS spectra of these catalysts show in Fig. 4a-c, respectively. As seen in Fig. 4a, the Mn 2p$_{3/2}$ spectra can be deconvoluted into three peaks at 640.1, 641.6 and 644.5 eV, which are attributed to the Mn^{2+}, Mn^{3+} and Mn^{4+} species, respectively [23–25]. It can be summarized that Mn_3O_4-3 exhibits the maximum surface molar ratio (0.256) of Mn^{4+}/Mn_{total} compared with other

catalysts (0.119–0.172) in Table S1, implying that more surface Mn species are in high valence state for Mn_3O_4-3. The Mn average oxidation state (AOS) from the splitting energy (ΔEs) of Mn 3s (Fig. 4b) further provides evidence of high valence state in Mn_3O_4-3. As shown in Fig. 4c, the O 1s XPS spectra are deconvoluted into three peaks centered at 529.5, 530.6 and 531.9 eV, corresponding to the lattice oxygen (O_{latt}), surface adsorbed oxygen (O_{ads}) and carbonate/water (O_{-OH}) species, respectively [26]. It could be seen that the surface of Mn_3O_4-3 possesses the highest O_{ads} ratio (0.275) compared to the other three catalysts (0.176–0.237) in Table S1, which is due to the existence of richer oxygen vacancies (V_O) and higher Mn^{4+} contents beneficial to the adsorption/activation of gas oxygen into reactive oxygen species [24].

In addition, the changed structural defects and surface chemical compositions also adjust the electronic atmosphere and coordination
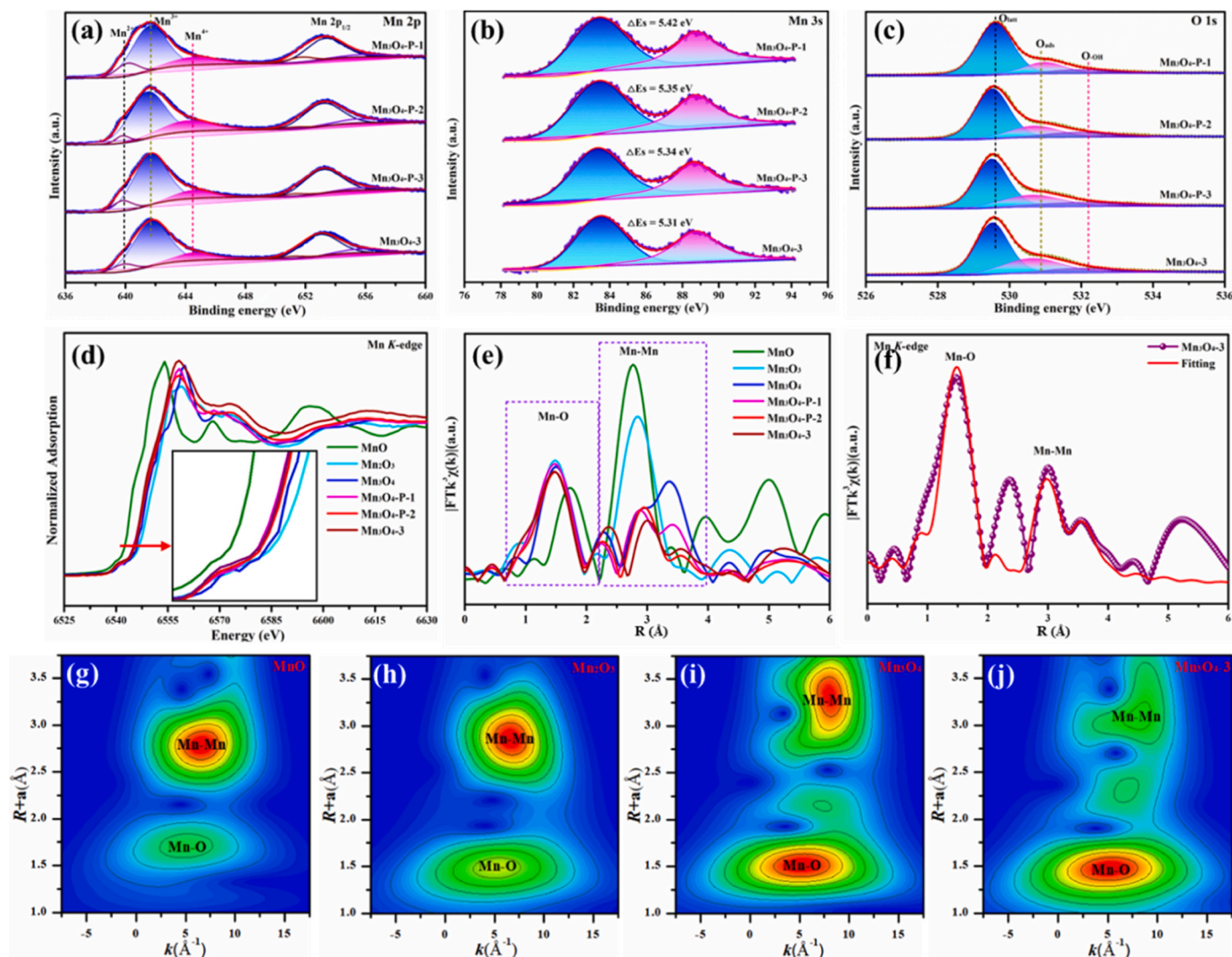
Fig. 4. (a) Mn 2p, (b) Mn 3s and (c) O 1s XPS spectra of Mn_3O_4-3 and Mn_3O_4-P-x catalysts. (d) Normalized XANES signals, (e) Fourier transform EXAFS spectra of Mn_3O_4-3, Mn_3O_4-P-2, Mn_3O_4-P-1 and references, as well as (f) R space fitting curves at the Mn K-edge of Mn_3O_4-3. Wavelet-transformed (WT)-EXAFS spectra of k^3-weighted Mn K-edge for (g) MnO, (h) Mn_2O_3, (i) Mn_3O_4 and (j) Mn_3O_4-3.

environment of neighboring atoms, which were further confirmed by X-ray absorption spectroscopy (XAS). According to the normalized Mn K-edge XANES curves (Fig. 4d) and wavelet-transformed (WT)-EXAFS spectra (Fig. 4g-j), three catalysts (Mn_3O_4-3, Mn_3O_4-P-2 and Mn_3O_4-P-1) tend to be the Mn_3O_4 crystal structure, and the Mn K-edge for Mn_3O_4-3 shows a relatively higher energy than that of other two catalysts, indicating that the Mn species in Mn_3O_4-3 maintain higher valence state. It has been reported that the strengthened peak of Mn-Mn$_{oct}$ in the edge-shared octahedra and the weakened peak of Mn-Mn$_{tet}$ in the corner-shared tetrahedra are attributed to the oxidization of Mn^{2+} [27]. As expected, Fourier transformed Mn K-edge EXAFS profiles in Fig. 4e reveal that there is the same phenomenon with strengthened Mn-Mn$_{oct}$ peak and the weakened Mn-Mn$_{tet}$ peak in Mn_3O_4-3 compared to the Mn_3O_4 reference, indicating the lower Mn^{2+} contents in accordance with the XPS results. R space fitting curves at the Mn K-edge (phase-uncorrected distances) of Mn_3O_4-3 with three main peaks at ~1.5, ~2.4 and ~3.0 Å are attributed to the Mn-O, Mn-Mn$_{oct}$ and Mn-Mn$_{tet}$, respectively [28]. As summarized in Table S3, the coordination numbers of Mn-O, Mn-Mn$_{oct}$ and Mn-Mn$_{tet}$ in Mn_3O_4-P-1 with worst catalytic performance are 4.2, 5.6 and 3.5, respectively, of which its Mn-Mn coordination numbers are lower than those in Mn_3O_4 reference (4.0, 6.0 and 5.9), suggesting the existence of unsaturated Mn defects. The

increased Mn-O coordination number may originate from the higher Mn^{2+} contents in Mn_3O_4-P-1. Notably, Mn_3O_4-3 with best catalytic performance presents the more lower coordination numbers of Mn-O (3.8), Mn-Mn$_{oct}$ (4.5) and Mn-Mn$_{tet}$ (2.5) than Mn_3O_4-P-1 and Mn_3O_4 reference, illustrating the simultaneous existence of enriched unsaturated Mn defects (V_{Mn}) and oxygen vacancies (V_O) [29]. The above enriched V_{Mn} and Vo results in Mn_3O_4-3 are basically consistent with the XPS results.

Considering the significant changes in the geometric structure and microscopic property, other physico-chemical properties over these catalysts were further characterized. As shown in Fig. S13, all these catalysts exhibit similar type IV with typical H3 hysteresis loop in the relative pressure range of 0.8–1.0, and its pore size distributions are concentrated in a small area (10.2–18.5 nm, Table S4), indicating the presence of mesoporous. The specific surface area (S_{BET}) values of these catalysts are relatively close to 22.33–27.34 m^2 g^{-1}, except for Mn_3O_4-P-2 (about 40.75 m^2 g^{-1}). Evidently, the as-obtained Mn_3O_4-3 presents a largest pore volume (0.213 cm^3 g^{-1}) compared to the Mn_3O_4-P-x catalysts (0.154–0.184 cm^3 g^{-1}), which is beneficial to the improved VOCs adsorption. Fig. S14 shows the H_2-TPR profiles of Mn_3O_4-3 and Mn_3O_4-P-x catalysts. It is observed that there are three reduction peaks at 187.5, 295.5 and 401 °C on Mn_3O_4-P-1, which are attributed to the reduction

process of adsorbed oxygen species, Mn^{4+} to Mn^{3+} and Mn^{3+} to Mn^{2+}, respectively [26,30]. Besides, the onset reduction peaks of adsorbed oxygen species and Mn^{4+} to Mn^{3+} on other catalysts with better catalytic activities remarkably shift to lower temperature position, especially Mn_3O_4-3, which suggests the better low-temperature reducibility and the effective reactivity of adsorbed oxygen species in Mn_3O_4-3. Mn_3O_4-3 also displays the strengthened intensity of latter two reduction peaks, demonstrating the more high-valence manganese in accordance with the XAS and XPS results. The adsorption and mobility ability of oxygen species over these catalysts are investigated by O_2-TPD in Fig. S15. The three major desorption areas appear at approximately 50–150 (O_I), 400–600 (O_{II}) and above 650 °C (O_{II}), attributed to surface adsorbed oxygen (O_2, O_2^-, O^-), surface lattice oxygen (O^{2-}) and bulk lattice oxygen [26,31–33]. The O_I species are related to the oxygen vacancy content and oxygen activation capacity, and the O_{II} species are related to the lattice oxygen migration capacity [26]. Distinctly, the O_I peak intensity on Mn_3O_4-3 is the largest among these four catalysts, which is attributed to the largest pore volume and the most sites (V_{Mn} and V_O) of adsorbed oxygen. Meanwhile, the higher intensity of O_{II} peaks signifies that unsaturated defects in Mn_3O_4-3 obviously induce the desorption of more surface lattice oxygen to form reactive oxygen species. The cyclic O_2-TPD curves further verify that Mn_3O_4-3 endows more better oxygen

activation capacity than Mn_3O_4-P-1 (Fig. S16). The TGA curves in Fig. S17 reveal that there are certain amounts of carbonate/water (O_{-OH}) species in these Mn_3O_4-3 and Mn_3O_4-P-x catalysts, and they have a well thermal stability at below 450 °C, which can well meet the operating requirements for photothermal OVOCs oxidation.

Additionally, to uncover the contributions of photocatalysis, physicochemical properties of these catalysts were further characterized. The light absorption ability of Mn_3O_4-3 and Mn_3O_4-P-x catalysts was detected by UV–vis DRS. As shown in Fig. S18, all the samples exhibit clear light absorption in both UV and visible light regions due to the inherent nature of dark-colored manganese oxides [11]. The Mn_3O_4-3 and Mn_3O_4-P-x show the strengthened light absorption ability in the visible light region, suggesting that its utilization of solar energy is effectively improved compared with Mn_3O_4-P-1 and Mn_3O_4-P-1 catalysts. As a result, there is a higher solar-driven-heating surface temperature (Fig. 3c) on Mn_3O_4-3 than other catalysts. According to the Tauc plots, the indirect energy bandgap (E_g) for Mn_3O_4-3, Mn_3O_4-P-3, Mn_3O_4-P-2 and Mn_3O_4-P-1 (Fig. 5a) is estimated to be 1.73, 1.91, 2.13 and 2.22 eV, respectively. Noteworthily, abundant unsaturated defects can availably shrink the E_g value, especially Mn_3O_4-3 with enriched V_{Mn} and V_O. Furthermore, the Mott-Schottky curves with the positive slopes (Fig. 5b, c, S19 and S20) confirm the feature of n-type semiconductors
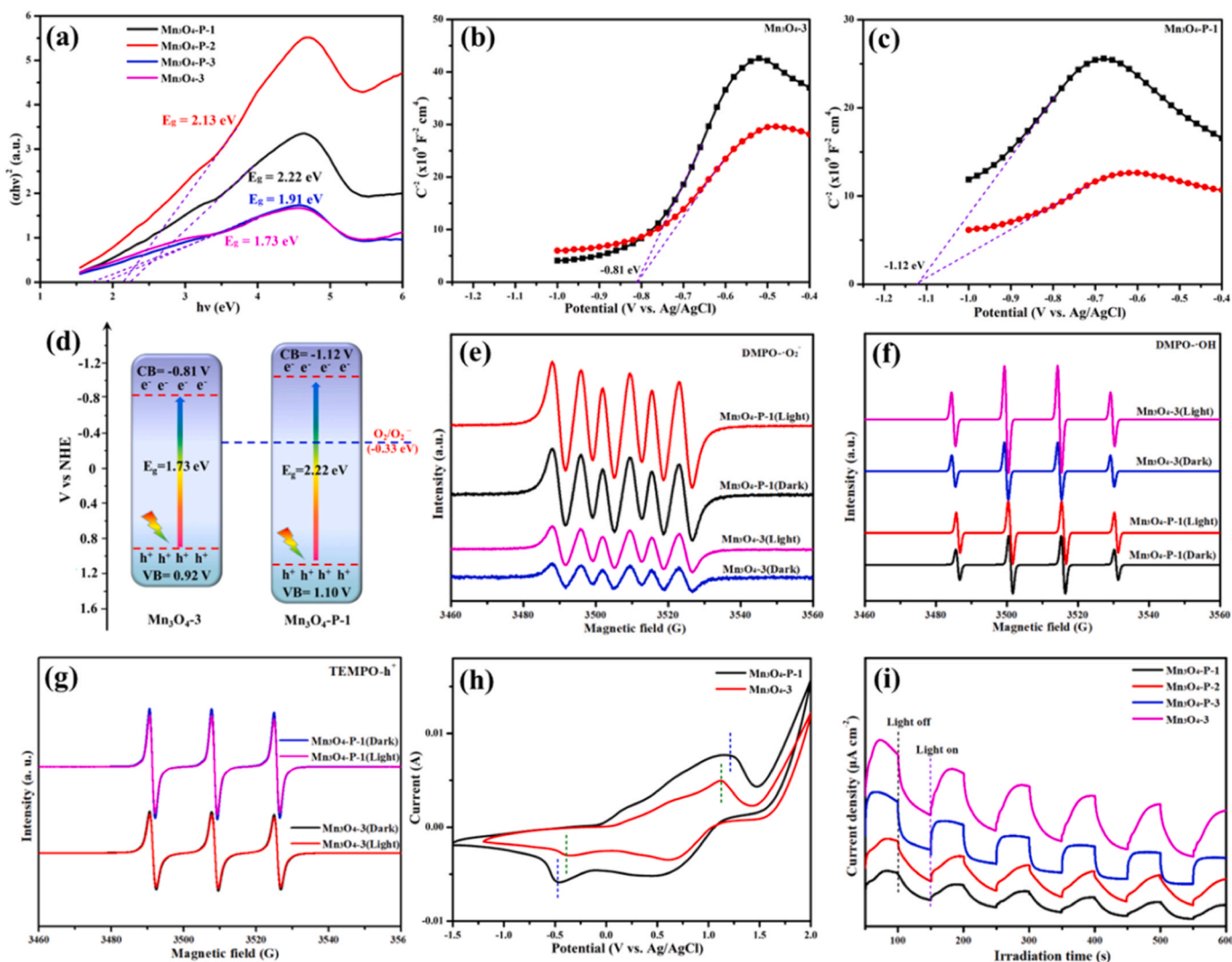
Fig. 5. (a) Tauc plots of $(\alpha h\nu)^2$ vs energy $h\nu$ for the indirect energy bandgaps, (b, c) Mott-Schottky curves and (d) energy band diagrams of Mn_3O_4-3 and Mn_3O_4-P-1 catalysts. EPR signals of (e) DMPO-$\bullet O_2^-$, (f) DMPO-$\bullet OH$ and (g) TEMPO-h^+ over Mn_3O_4-3 and Mn_3O_4-P-1 under dark/light conditions, (h) CV curves of Mn_3O_4-3 and Mn_3O_4-P-1 catalysts at a scan rate of 0.1 mV s^{-1} as well as (i) transient photocurrent responses to light on/off.

on these catalysts. Their flat-band potentials of Mn_3O_4-3, Mn_3O_4-P-3, Mn_3O_4-P-2 and Mn_3O_4-P-1 are measured to be -0.81, -0.99, -1.04 and -1.12 V (vs Ag/AgCl), respectively, corresponding Fermi levels (E_f) are located at -0.61, -0.79, -0.84 and -0.92 V (vs NHE). In general, the conduction band potential (E_{CB}) in the n-type semiconductor is 0.1–0.3 eV lower than the flat-band potential [34]. Therefore, the E_{CB} of Mn_3O_4-3, Mn_3O_4-P-3, Mn_3O_4-P-2 and Mn_3O_4-P-1 could be estimated to be -0.81, -0.99, -1.04 and -1.12 V (vs NHE), respectively, and their corresponding E_{VB} values occur at about 0.92, 0.92, 1.09 and 1.10 V (vs NHE) (based on the formula $E_{CB} = E_{VB} - E_g$). Based on the above results, the detailed energy band diagrams of various catalysts are shown in Fig. 5d and S21. According to the redox potentials of $O_2/\bullet O_2^-$ (-0.33 eV) and $H_2O/\bullet OH$ (2.38 eV), superoxide radicals ($\bullet O_2^-$) are generated by photoexcited electron reduction of molecular oxygen ($O_2 + e^- \to \bullet O_2^-$) in these catalysts, whereas hydroxyl radicals ($\bullet OH$) are more difficultly produced by photoexcited hole oxidation of water molecules ($H_2O + h^+ \to H^+ + \bullet OH$) due to its redox potential no located within energy bandgaps [26]. Surprisingly, the characteristic signal peaks of both DMPO-$\bullet O_2^-$ and DMPO-$\bullet OH$ in the Mn_3O_4-3 and Mn_3O_4-P-1 are indeed observed, and its signal intensities of $\bullet O_2^-$ and $\bullet OH$ radicals are further enhanced after irradiation for 20 min (Fig. 5e, f), implying the more generation and transformation of reactive oxygen species (ROS, $\bullet O_2^-$ and $\bullet OH$) by photogenerated carriers (electrons and holes) under light conditions, indicating that the $\bullet O_2^-$ and $\bullet OH$ radicals could participate in the photothermal synergistic catalytic oxidation reaction [5]. However, the signal intensities of $\bullet O_2^-$ radicals in Mn_3O_4-3 is distinctly lower than those in Mn_3O_4-P-1, which may be due to the direct dissociation for O_2 in defect-rich Mn_3O_4-3 (proved by DFT calculations in Fig. 7i). Therefore, it could be speculated that the generation of $\bullet OH$ radicals in Mn_3O_4-3 and Mn_3O_4-P-1 is ascribed to the reduction of O_2 and then the dissociation of peroxide species ($O_2 + H^+ + e^- \to OOH$, $OOH + H^+ + e^- \to O + H_2O$, $O + H^+ + e^- \to OH$) [35,36]. The signal peaks of $\bullet OH$ radicals on Mn_3O_4-3 are higher than those on Mn_3O_4-P-1 after light irradiation, suggesting its higher oxidation ability in comparison to Mn_3O_4-P-1. Moreover, the signal peaks of TEMPO-h^+ in Mn_3O_4-3 and Mn_3O_4-P-1 become weaker after irradiation for 20 min (Fig. 5g), because the trapping agent was consumed by holes (TMEPO + $h^+ \to$ TEMPO$^+$) [37,38]. The signal of TEMPO-h^+ in Mn_3O_4-3 is higher than that in Mn_3O_4-P-1 under light irradiation, indicating the more generation of holes (h^+) in Mn_3O_4-3.

The redox abilities of Mn_3O_4-3 and Mn_3O_4-P-1 were also evaluated by CV measurements at a scan rate of 0.1 mV s^{-1}, as shown in Fig. 5h. As seen, the CV curves on Mn_3O_4-3 and Mn_3O_4-P-1 display a pair of redox peaks, and the potential difference between oxidation and reduction peaks on Mn_3O_4-3 is lower than that of Mn_3O_4-P-1, which is consistent with the smaller E_g value and indicates more excellent redox ability on Mn_3O_4-3. The transient photocurrent response and EIS measurements were conducted to explore the separation of photogenerated charge carriers (h^+ and e^-). As shown in Fig. 5i, the variation tendency of photocurrent intensity follows the order of Mn_3O_4-3 > Mn_3O_4-P-3 > Mn_3O_4-P-2 > Mn_3O_4-P-1, inferring that the separation of photogenerated charge carriers can significantly be enhanced by unsaturated coordination defects on manganese oxides. Besides, Mn_3O_4-3 exhibits the smallest arc radius than other three Mn_3O_4-P-x catalysts (Fig. S22), suggesting the lowest charge-transfer resistance on Mn_3O_4-3 facilitating the rapid transfer of photogenerated charge carriers. Overall, these results confirm that the abundant unsaturated coordination defects on Mn_3O_4-3 not only effectively narrow energy bandgap for strengthening light response ability, but also improve the separation and transfer of photogenerated electrons and holes.

3.4. Photothermal reaction mechanism

To explore the role of oxygen species and the detailed photothermal reaction process of ethyl acetate oxidation on the catalyst surface, in-situ DRIFTS studies were conducted under different conditions. Firstly, the adsorption/oxidation of ethyl acetate on Mn_3O_4-P-1 with various time were investigated at 120 °C in the absence of O_2, as shown in Fig. 6a, b. Several characteristic bands of ethyl acetate and related intermediate species are observed on the surface, such as ethyl acetate (1049, 1240 and 1697 cm^{-1}) [4,5,39–41], methanol (~1022 cm^{-1}) [1], ethanol (~1095 and ~1382 cm^{-1}) [34], formate (~1309 cm^{-1}) [42], aldehyde (1750–1780 cm^{-1}) [43], ethylene (912 and 979 cm^{-1}) [34] and carboxylic acid (~1432 and ~1556 cm^{-1}) species [4,44,45]. The detail bands related to the adsorbed intermediate species are summarized in Table S5. The negative bands centered at 3400–3800 cm^{-1} are attributed to the ν(O-H) stretching vibrations of surface hydroxyl groups, and surface hydroxyl groups are more easily interacted with adsorbed ethyl acetate to dissociate acetic acid and ethanol [1]. Importantly, the absorption band intensity of ethyl acetate and intermediate species on Mn_3O_4-P-1 increases with the increased time under the dark/light conditions (Fig. 6c), and the ethanol/carboxylic acid are the dominant surface intermediates due to its intense characteristic bands, further indicating the deep removal of surface ethanol/carboxylic acid as the rate-determining step. When the light source is introduced into reaction system in the absence of oxygen, the characteristic band of ester linkage on ethyl acetate is no observed on the surface, and the characteristic band intensity of various intermediate species gradually become stronger than that in the dark, indicating that the introduction of light accelerates a decomposition rate of ethyl acetate to generate intermediates, especially ethanol/carboxylic acid (Fig. 6c). Then, the adsorption/oxidation of ethyl acetate on Mn_3O_4-P-1 with various time were investigated at 120 °C in the presence of O_2, as shown in Fig. 6d, e. In-situ DRIFTS spectra on Mn_3O_4-P-1 reveal that the new ethylene production is immediately detected after light irradiation, while the band intensity of major intermediate species under light irradiation obviously decreases compared with that in the dark (Fig. 6f). There are similar rules in the in-situ DRIFTS spectra on Mn_3O_4-3, as shown in Fig. 6g-i. Additionally, it can be found that ethylene production is generated in the absence of O_2, implying that the breakage ethyl ($CH_3CH_2\bullet$) group of absorbed ethyl acetate molecule on the Mn_3O_4-P-1 could react with surface lattice oxygen to form ethylene. Meanwhile, all in-situ DRIFTS spectra in light irradiation appear the characteristic bands of ethylene, inferring that the C-H band in ethyl group ($CH_3CH_2\bullet$) may be directly broken via photogenerated-electron attack, or via reacting with the migrated lattice oxygen due to the light-excitation effect.

The variation tendency of typical intermediates at different conditions are displayed in Fig. S23-S27. In terms of methanol (~1022 cm^{-1}), introducing light irradiation can increase its band intensity in the presence of O_2 over Mn_3O_4-P-1 than that in the dark, otherwise, its band intensity in other conditions will decrease (Fig. S23). This more accumulation of methanol on the surface of Mn_3O_4-P-1 further verifies the evaluation result of higher by-product methanol concentration. Nevertheless, ethanol (~1382 cm^{-1}) and carboxylic acid (~1432 and ~1556 cm^{-1}) species in the absence of O_2 over Mn_3O_4-P-1 with poor catalytic activity are more produced under light irradiation than those in the dark (Fig. S24, S26 and S27), which is due to the hydrolysis/dissociation of ethyl acetate to ethanol and carboxylic acid, subsequently more difficult to convert to other intermediates without sufficient reactive oxygen species. Furthermore, the main intermediates absorbed on the surface of Mn_3O_4-3 with abundant defects and outstanding catalytic activity are less accumulated than those on Mn_3O_4-P-1, meaning that surface main intermediates can be easily interacted with reactive oxygen species and rapidly converted into the H_2O and CO_2.

To systematically elucidate the role of defect sites for the O_2 activation and ethyl acetate dissociation/hydrolysis, a series of defective Mn_3O_4(110) models were constructed and optimized via density functional theory (DFT) calculations. Firstly, O_2 molecule is absorbed on the surface of defect-free Mn_3O_4(110), Mn_3O_4(110)-V_O with one O vacancy, Mn_3O_4(110)-V_{Mn} with one Mn vacancy and Mn_3O_4(110)-V_{2O} with two O vacancies, respectively, as shown in Fig. S28. The adsorption energies
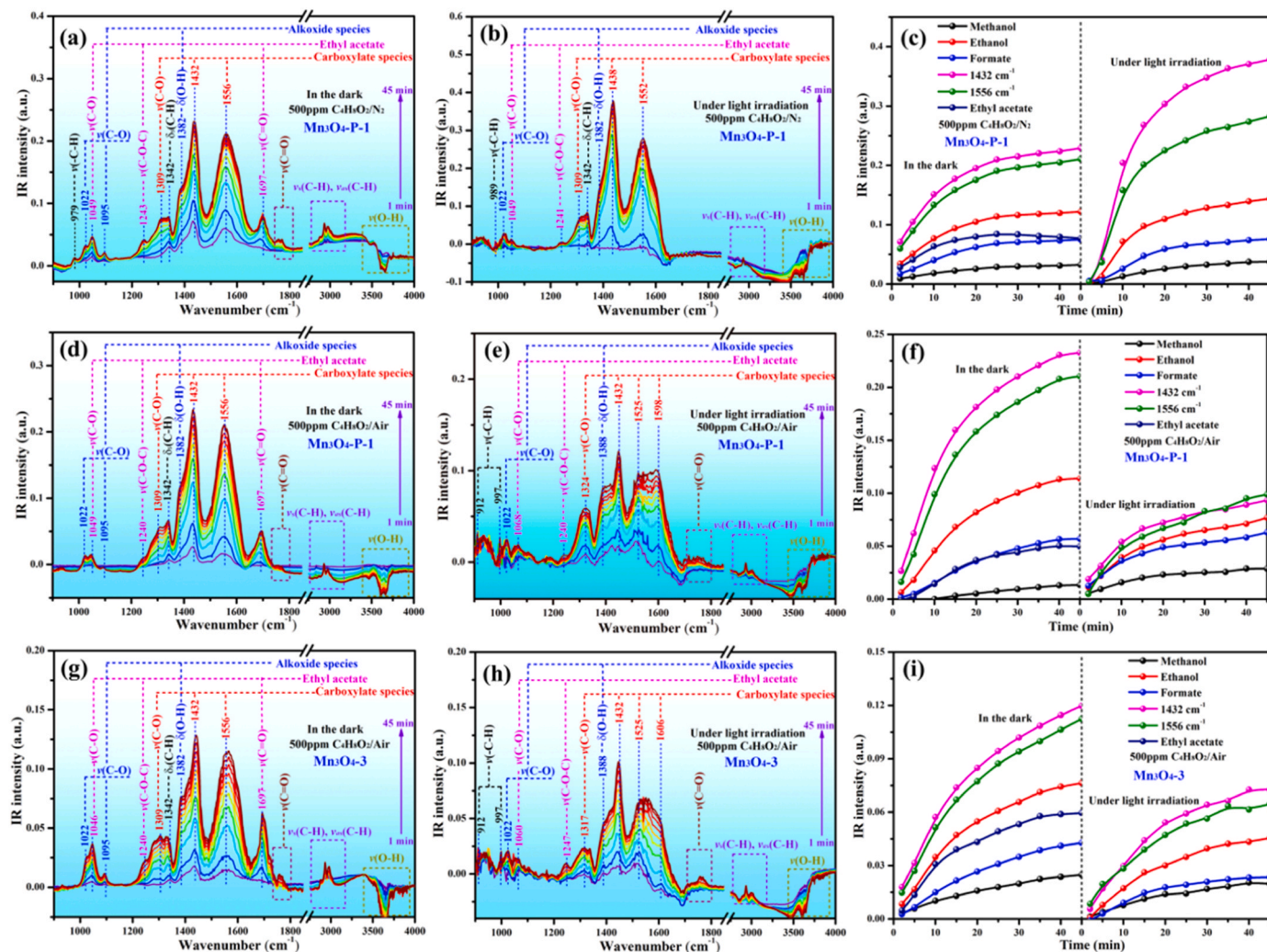
Fig. 6. In-situ DRIFTS spectra of ethyl acetate oxidation as a function of time exposed to 500 ppm ethyl acetate/N$_2$ under the conditions of (a) dark and (b) light irradiation, as well as 500 ppm ethyl acetate/air atmosphere under the conditions of (d) dark and (e) light irradiation over Mn$_3$O$_4$-P-1 catalyst. In-situ DRIFTS spectra of ethyl acetate oxidation exposed to 500 ppm ethyl acetate/air under the conditions of (g) dark and (h) light irradiation over Mn$_3$O$_4$-3 catalyst. (c, f and i) Plots of IR signal intensities of surface organic species involving methanol (~1022 cm^{-1}), ethanol (~1382 cm^{-1}), formate (~1309 cm^{-1}), carboxylic acid (~1432 and ~1556 cm^{-1}) and ethyl acetate (~1697 cm^{-1}) versus time under different conditions.

(E_{ads}) of O$_2$ molecule on defect-free Mn$_3$O$_4$(110), Mn$_3$O$_4$(110)-V$_O$, Mn$_3$O$_4$(110)-V$_{Mn}$ and Mn$_3$O$_4$(110)-V$_{2O}$ are calculated to be − 4.512, − 3.994, − 2.531 and − 7.959 eV, respectively. As displayed in Fig. 7a-c, the O-O band distances (d_{O2}) of absorbed O$_2$ on defect-free Mn$_3$O$_4$(110), Mn$_3$O$_4$(110)-V$_O$ and Mn$_3$O$_4$(110)-V$_{Mn}$ are elongated from 1.23 Å in isolated state to 1.482, 1.492 and 1.470 Å, respectively. The O-O band of absorbed O$_2$ on Mn$_3$O$_4$(110)-V$_{2O}$ is elongated to break and placed at the surrounding manganese sites near two oxygen vacancies (Fig. 7d), meaning a superior activation ability of O$_2$. However, in comparison to defect-free Mn$_3$O$_4$(110), the Mn$_3$O$_4$(110)-V$_{Mn}$ shows the shorter d_{O2} and weaker E_{ads}, suggesting the opposite effect on the O$_2$ adsorption. Charge density differences and Bader analyses and density of states (DOS) were implemented to investigate the degree of activation of O$_2$ molecules on different defective structures in deeper detail. After that, charge density differences and Bader analyses reveal the charge redistributions and significant charge transfers from defective structures to O$_2$ molecules (Fig. 7a-d). The charge transfer amounts of defect-free Mn$_3$O$_4$(110), Mn$_3$O$_4$(110)-V$_O$, Mn$_3$O$_4$(110)-V$_{Mn}$ and Mn$_3$O$_4$(110)-V$_{2O}$ to O$_2$ molecules are 1.108, 1.113, 1.048 and 2.274 |e|, respectively. The Mn$_3$O$_4$(110)-V$_{2O}$ exhibits a significantly higher charge transfer than other defective structures, suggesting the more excess electrons on Mn$_3$O$_4$(110)-V$_{2O}$ transferring to O$_2$ molecule. More importantly, the

DOS of adsorbed O$_2$ molecule on defect-free Mn$_3$O$_4$(110) exhibits the lower hybridization degree between Mn 3d orbitals and O 2p orbitals at Fermi levels in comparison to those of O-vacancy Mn$_3$O$_4$(110)-V$_O$ and Mn$_3$O$_4$(110)-V$_{2O}$ (Fig. S29), indicating that O-vacancy structure can better activate O$_2$ molecules and form a stronger interaction. Finally, the thermodynamic energy barriers and corresponding atomic structures of initial state (IS, O$_2$ *), transition sate (TS) and final sate (FS, O*−O*/ O*+O*) are presented in Fig. 7i and S30. The adsorption geometry of O$_2$ molecules on defect-free Mn$_3$O$_4$(110) is transformed from end-on-type to side-on-type configuration, indicating that the side-on O$_2$ adsorption on the catalyst is more stable and can effectively strengthen the O-O bond distance (Fig. S30). As a comparison, the barrier energies (ΔE) of O$_2$ activation/dissociation on structure models follow the sequence: Mn$_3$O$_4$(110)-V$_{2O}$ (−0.06 eV) < Mn$_3$O$_4$(110)-V$_O$ (0.33 eV) < Mn$_3$O$_4$(110)-V$_{Mn}$ (1.05 eV) < defect-free Mn$_3$O$_4$(110) (1.45 eV). Both Mn and O vacancies on structure models would decrease the barrier energies of O$_2$ activation/dissociation, and O$_2$ can be directly dissociated on Mn$_3$O$_4$(110)-V$_{2O}$ with two O vacancies. These above calculation results powerfully confirm that abundant O vacancies on the manganese oxides will be beneficial to the more supplying electrons to O$_2$ molecule and lower O$_2$ dissociation barrier energy.

Besides, ethyl acetate (C$_4$H$_8$O$_2$) molecule is absorbed on the surface
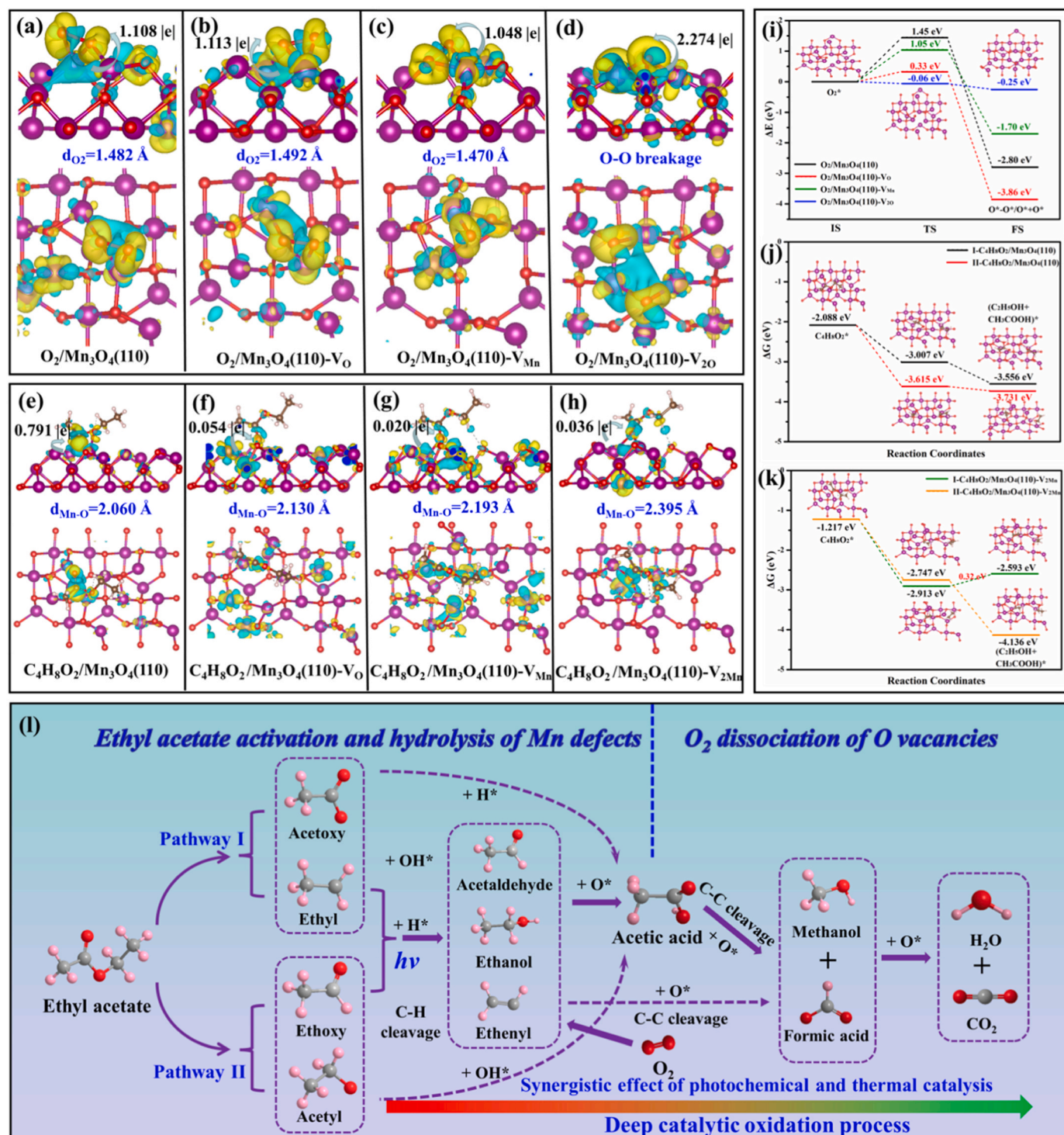
Fig. 7. Charge density differences, charge transfer amounts and bond distances on (a) O_2/Mn_3O_4(110), (b) O_2/Mn_3O_4(110)-V_O, (c) O_2/Mn_3O_4(110)-V_{Mn}, (d) O_2/Mn_3O_4(110)-V_{2O}, (e) $C_4H_8O_2$/Mn_3O_4(110), (f) $C_4H_8O_2$/Mn_3O_4(110)-V_O, (g) $C_4H_8O_2$/Mn_3O_4(110)-V_{Mn} and (g) $C_4H_8O_2$/Mn_3O_4(110)-V_{2Mn}, where yellow and cyan denote positive and negative charge populations, respectively (The isosurface value is set to 0.005 e/$Å^3$). (i) The barrier energies of O_2 activation/dissociation on the difference structural model surfaces (IS: initial state; TS: transition state; FS: final state). Calculated energetic routes of ethyl acetate adsorption and dissociation on the (j) Mn_3O_4(110) and (k) Mn_3O_4(110)-V_{2Mn}. (l) The proposed reaction mechanism for concentrated solar-heating photothermal catalysis over manganese oxides with unsaturated coordination defects (Mn and O).

of defect-free Mn_3O_4(110), Mn_3O_4(110)-V_O, Mn_3O_4(110)-V_{Mn} and Mn_3O_4(110)-V_{2Mn} with two Mn vacancies, respectively, as shown in Fig. S31. The E_{ads} values of $C_4H_8O_2$ molecule on defect-free Mn_3O_4(110), Mn_3O_4(110)-V_O, Mn_3O_4(110)-V_{Mn} and Mn_3O_4(110)-V_{2Mn} are respectively calculated to be -2.088, -2.453, -1.747 and -1.217 eV, and its charge transfer amounts to $C_4H_8O_2$ molecules are

0.791, 0.054, 0.020 and 0.036 |e|, respectively. The $C_4H_8O_2$ molecule is attached to two Mn atoms on the defect-free Mn_3O_4(110) structure, while the others are attached to one Mn atom on defective Mn_3O_4(110) structures (Fig. 7e-h). The stronger E_{ads} and more charge transfer amount are not a good indication of the activation of $C_4H_8O_2$ molecules due to the influence of itself structural models and interatomic forces in

complex $C_4H_8O_2$ molecule. However, in comparison to defect-free $Mn_3O_4(110)$ (2.060 Å), the elongated Mn-O band distances (d_{Mn-O}) on defective $Mn_3O_4(110)$ structures imply a better activation of $C_4H_8O_2$ molecule especially $Mn_3O_4(110)$-V_{2Mn}, which is further verified by DOS after adsorbed $C_4H_8O_2$ molecule (Fig. S32). Moreover, Fig. 7j shows that there are two possible pathways for $C_4H_8O_2$ dissociation/hydrolysis on defect-free $Mn_3O_4(110)$. I (pathway I) represents the $C_4H_8O_2 \rightarrow C_4H_8O_2$ * → $(CH_3CH_2\bullet + CH_3COO\bullet)$* → $(CH_3CH_2OH + CH_3COOH)$* process, and II (pathway II) represents the another $C_4H_8O_2 \rightarrow C_4H_8O_2$ * → $(CH_3CH_2O\bullet + CH_3CO\bullet)$* → $(CH_3CH_2OH + CH_3COOH)$* process. According to the Gibbs-free-energy change (ΔG) of each step, it can be seen that the $C_4H_8O_2$ dissociation/hydrolysis on $Mn_3O_4(110)$-V_O and $Mn_3O_4(110)$-V_{Mn} can respectively follow the pathway I and pathway II, and need to overcome the ΔG values of 0.485 and 1.153 eV (Fig. S33 and S34), respectively. The pathway II could be relatively more easily for $C_4H_8O_2$ dissociation/hydrolysis to form CH_3CH_2OH and CH_3COOH on $Mn_3O_4(110)$-V_{2Mn}, while its pathway I of $C_4H_8O_2$ dissociation/hydrolysis must cross the ΔG of 0.32 eV (Fig. 7k). Therefore, the formation of enriched Mn defects on the manganese oxides plays a more important role for the $C_4H_8O_2$ dissociation and hydrolysis into intermediates (ethanol and acetic acid) than O vacancies.

Combined with the above DFT calculations and in-situ DRIFTS results, the main reaction pathways of ethyl acetate oxidation and the role of unsaturated coordination defects (Mn and O) in photothermal catalytic processes are summarized in Fig. 7l. Firstly, the initial reaction pathways (Pathway I and II) of ethyl acetate decomposition are via the breaking of C-O bonds in the synergistic effect of photothermal and thermal catalysis, generating ethyl ($CH_3CH_2\bullet$) and acetoxy ($CH_3COO\bullet$), acetyl ($CH_3CO\bullet$) and ethoxy ($CH_3CH_2O\bullet$) groups, respectively [46]. In a light irradiation environment, most of the C_2 groups would be formed the ethanol, acetic acid, aldehyde and ethylene via a series of hydrolysis/oxidation reactions (+ H*, + OH* and C-H cleavage), in which the formation of ethanol, aldehyde and ethylene are partially oxidized into acetic acid. Subsequently, the above C_2 species would be further decomposed to C_1 species (methanol and formate) via the process of C-C cleavage and reacted with oxygen species (O*, O_2^-* and OH*), following to deeply oxidize into inorganic products CO_2 and H_2O. During the ethyl acetate oxidation, the photogenerated carriers in photothermal catalysis can react with ethyl acetate, H_2O/OH^- and O_2 to generate the active ethyl acetate ($C_4H_8O_2$ *) and reactive oxygen species ($\bullet OH$ and $\bullet O_2^-$). The existence of more Mn defects on Mn_3O_4-3 mainly facilitates the active $C_4H_8O_2$ * hydrolysis into key intermediates (ethanol and acetic acid). Meanwhile, the formation of enriched O vacancies on Mn_3O_4-3 plays significant role in enhancing the activation ability of oxygen species (O_2 and $\bullet O_2^-$) toward highly activated O* , promoting the surface deep oxidation process of various intermediates. However, ethyl acetate oxidation in thermocatalysis is more inclined to follow the following process (Pathway II): $C_4H_8O_2$ * → $(CH_3CH_2O\bullet + CH_3CO\bullet)$* → $(CH_3CH_2OH + CH_3CHO + CH_3COOH)$* → $(CH_3OH + HCOOH)$* → CO_2 + H_2O.

3.5. Role of photocatalysis and light-driven photothermocatalysis

Combined with the above catalytic activities and physico-chemical characterizations, it could be deduced that the coexistence of photocatalysis, thermocatalysis and photoactivation on Mn_3O_4-based catalysts synergistically participates in ethyl acetate oxidation reaction, and therefore contributes to the outstanding activity for solar-heating photothermal OVOCs degradation [15]. Firstly, the inferior catalytic activities of Mn_3O_4-based catalysts under non-concentrated/weak sunlight irradiation reveal that photocatalysis plays minor roles in the ethyl acetate oxidation. The light irradiation induces the more generation of $\bullet O_2^-$ and $\bullet OH$ radicals, and excites the more charge carriers (e^- and h^+) involving in photocatalysis. Secondly, solar-driven thermalocatalysis makes a major contribution on the enhanced photothermal performances for ethyl acetate oxidation. Strong light absorption in full solar

spectrum on Mn_3O_4-3 catalyst would trigger the higher solar-driven-heating temperature depending on its smaller energy bandgap, and further improve the ethyl acetate conversion and CO_2 yield. Certainly, the excellent catalytic activity on Mn_3O_4-3 catalyst is attributed to the chemical compositions/defects (Mn^{4+} and Vo), oxygen activation and redox abilities. Finally, photoactivation also plays an important role in the activation of lattice oxygen to break target gas via the light-excitation effect/attack.

At last, the cyclicity and stability experiments of as-prepared Mn_3O_4-3 catalyst were further investigated, as shown in Fig. S35. After manifold cycles and long-time stability tests, the solar-heating photothermal ethyl acetate conversion on Mn_3O_4-3 can maintain at approximately 96 % under simulated solar irradiation. Chemical properties of used Mn_3O_4-3 after long-time stability experiment were also characterized by XPS and EPR instruments. It should be noted that surface compositions of used Mn_3O_4-3 have changed markedly in comparison to fresh Mn_3O_4-3 sample, as displayed in Fig. 8a-c. The proportion of surface Mn^{4+} ions (Mn^{4+}/Mn_{total} = 0.211) on the Mn 2p XPS spectrum of used Mn_3O_4-3 is decreased than fresh Mn_3O_4-3 (0.276) in Fig. 8a, which could be affirmed by the increased ΔEs value (about 5.52 eV) of Mn 3s (Fig. 8b). Contrarily, surface adsorbed oxygen (O_{ads}) and carbonate/water (O_{-OH}) species on the used Mn_3O_4-3 are increased to 0.307 and 0.169 (Fig. 8c), respectively, which may be due to the structural changes and adsorbed water molecules from the reaction process of ethyl acetate oxidation. The more surface Mn^{4+} reduced to Mn^{3+} on the used Mn_3O_4-3 further leads to the larger formation of oxygen vacancies than fresh Mn_3O_4–3 (Fig. 8d).

4. Conclusion

In summary, we developed an optical concentrator-assisted photothermal system with photothermal (Mn_3O_4-based) catalysts for solar-heating OVOCs oxidation, of which defective Mn_3O_4-based photothermal catalysts were synthesized via solvent- and template-induced Mn-BTC isomers as sacrificial templates. Compared with traditional thermal catalysis, the as-obtained Mn_3O_4-3 catalyst displayed well photothermal catalytic activity, CO_2 yield and stability under weak simulated sunlight even natural sunlight irradiation, especially ethyl acetate conversion increased from 68 % to about 97 %. The Mn_3O_4-3 catalyst demonstrated good redox performance, more surface chemical active-compositions and excellent optical-electrical properties. In addition, light irradiation could affect the lattice oxygen migration and provoke the C-H breakage of ethyl group ($CH_3CH_2\bullet$) from ethyl acetate dissociation. It was testified that the existence of Mn defects on Mn_3O_4-based catalysts mainly facilitates the active $C_4H_8O_2$ * hydrolysis into key intermediates, and the formation of O vacancies plays significant role in enhancing the O_2 activation/dissociation toward highly activated O* participating in the surface deep oxidation process of various intermediates. Therefore, the enhancement of photothermal catalytic activity of ethyl acetate oxidation may be the result of synergistic effect of Mn defects and O vacancies. This work puts forward an important step for the practical application in controlling VOCs fields via natural sunlight-driven multiply catalysis.

CRediT authorship contribution statement

Shengpeng Mo: Conceptualization, Data curation, Formal analysis, Funding acquisition, Methodology, Writing – original draft. **Xin Zhao:** Conceptualization, Data curation, Formal analysis, Investigation, Methodology, Validation. **Lili Huang:** Investigation, Methodology, Validation. **Jiangjing Zhou:** Investigation, Validation, Visualization. **Shuangde Li:** Investigation, Validation, Software, Writing – review & editing. **Ruosi Peng:** Investigation, Visualization. **Zhihong Tu:** Investigation, Methodology. **Lei Liao:** Investigation, Visualization. **Qinglin Xie:** Funding acquisition, Investigation, Supervision. **Yunfa Chen:** Investigation, Validation. **Yanan Zhang:** Funding acquisition,
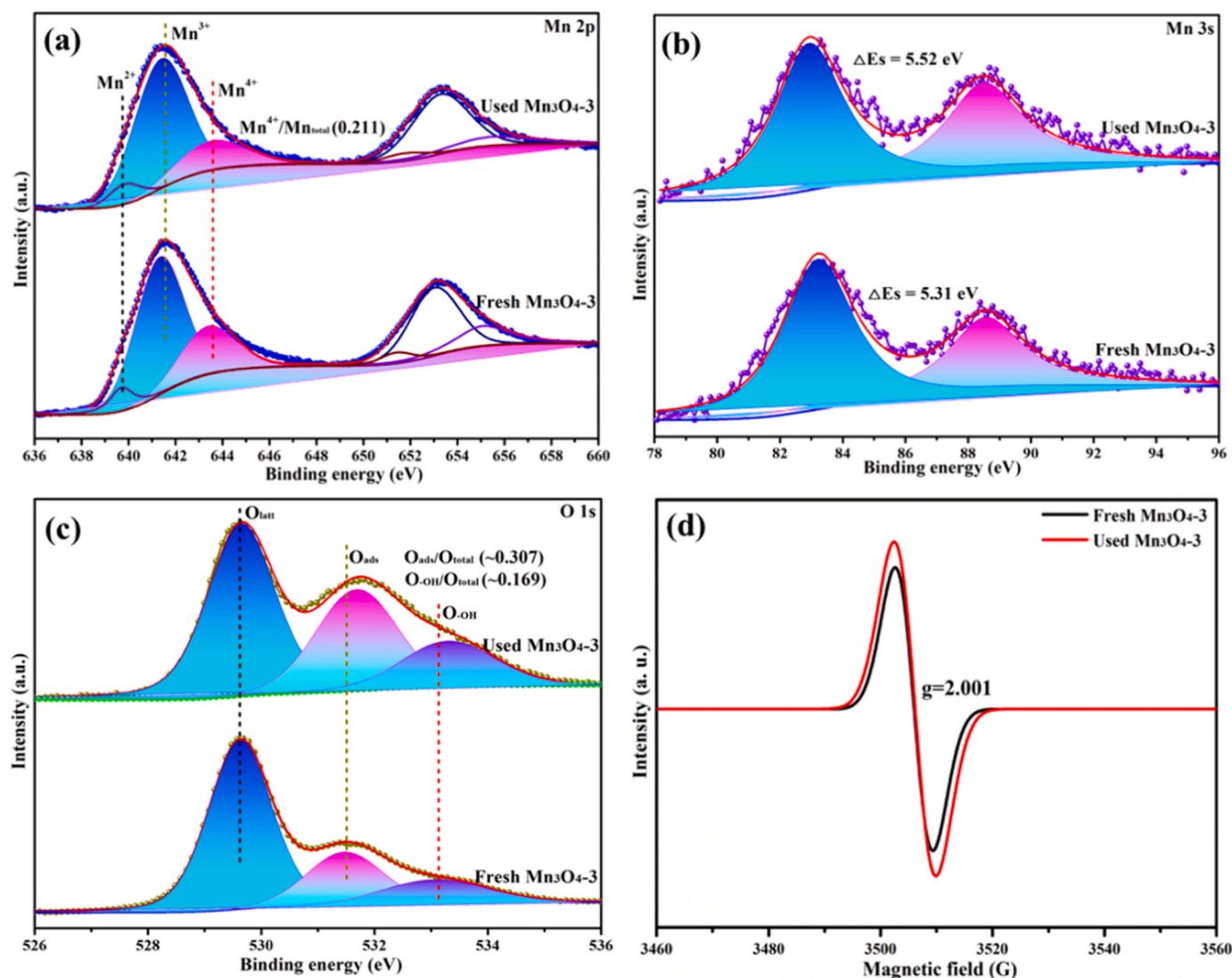
Fig. 8. (a) Mn 2p, (b) Mn 3s, (c) O 1s XPS spectra and (d) EPR signals of fresh and used Mn_3O_4-3 catalysts.

Investigation, Validation, Visualization, Writing – review & editing. **Daiqi Ye:** Investigation, Supervision.

Declaration of Competing Interest

The authors declared that they have no conflicts of interest to this work. We declare that we do not have any commercial or associative interest that represents a conflict of interest in connection with the work submitted.

Data availability

Data will be made available on request.

Appendix A. Supporting information

Supplementary data associated with this article can be found in the online version at doi:10.1016/j.apcatb.2023.123435.

References

[1] Z. Shen, E. Gao, X. Meng, J. Xu, Y. Sun, J. Zhu, J. Li, Z. Wu, W. Wang, S. Yao, Q. Dai, Mechanistic insight into catalytic combustion of ethyl acetate on modified CeO_2 nanobelts: hydrolysis-oxidation process and shielding effect of acetates/ alcoholates, Environ. Sci. Technol. 57 (2023) 3864–3874.

[2] Y. Zhang, Y. Li, J. Wu, H. Cao, L. Zhang, La doping of manganese oxide leads to a dramatically promoted catalytic performance for UV–visible-infrared photothermocatalytic ethyl acetate abatement, Appl. Surf. Sci. 615 (2023), 156334.

[3] C. Shan, Y. Wang, J. Li, Q. Zhao, R. Han, C. Liu, Q. Liu, Recent advances of VOCs catalytic oxidation over spinel oxides: catalyst design and reaction mechanism, Environ. Sci. Technol. 57 (2023) 9495–9514.

[4] N. Dong, Q. Ye, D. Zhang, Y. Xiao, H. Dai, Reduced graphene oxide as an effective promoter to the layered manganese oxide-supported Ag catalysts for the oxidation of ethyl acetate and carbon monoxide, J. Hazard. Mater. 431 (2022), 128518.

[5] X. Wang, L. Wu, Z. Wang, Y. Feng, Y. Liu, H. Dai, Z. Wang, J. Deng, Photothermal synergistic catalytic oxidation of ethyl acetate over MOFs-derived mesoporous N-TiO_2 supported Pd catalysts, Appl. Catal. B 322 (2023), 122075.

[6] Y. Shen, J. Deng, X. Hu, X. Chen, H. Yang, D. Cheng, D. Zhang, Expediting toluene combustion by harmonizing the Ce-O strength over co-doped CeZr oxide catalysts, Environ. Sci. Technol. 57 (2023) 1797–1806.

[7] L. Liao, X. Ding, J. Li, L. Huang, M. Zhang, Y. Fan, X. Zhou, Y. Zhang, S. Mo, Q. Xie, D. Ye, Constructing MOFs-derived Co_3O_4 microsphere with atomic p-n

homojunction as an efficient photothermal catalyst for boosting ethyl acetate oxidation under light irradiation, Sep. Purif. Technol. 309 (2023), 122939.

[8] Y. Zhang, Y. Zhu, Y. Fan, Z. Zhu, L. Liao, S. Mo, L. Zhang, S. Tang, X. Zhou, Highly active nanostick-assembled TiO$_2$@MnO$_x$ hollow-sphere structure for photothermocatalysis of ethyl acetate and NO with free-ammonia at low temperature: resistence, key reaction steps and mechanisms, Appl. Surf. Sci. 607 (2023), 154887.

[9] Y. Yang, S. Zhao, L. Cui, F. Bi, Y. Zhang, N. Liu, Y. Wang, F. Liu, C. He, X. Zhang, Recent advancement and future challenges of photothermal catalysis for VOCs elimination: from catalyst design to applications, Green. Energy Environ. 8 (2023) 654–672.

[10] C. Feng, Y. Bi, C. Chen, S. Li, Z. Wang, H. Xin, Y. Pan, F. Liu, Y. Lu, Y. Liu, R. Zhang, X. Li, Urea-H$_2$O$_2$ defect engineering of δ-MnO$_2$ for propane photothermal oxidation: structure-activity relationship and synergetic mechanism determination, J. Colloid Interface Sci. 641 (2023) 48–58.

[11] S. Jiang, C. Li, Y. Muhammad, Y. Tang, R. Wang, J. Li, J. Li, Z. Zhao, Z. Zhao, Solvent-induced fabrication of Cu/MnO$_x$ nanosheets with abundant oxygen vacancies for efficient and long-lasting photothermal catalytic degradation of humid toluene vapor, Appl. Catal. B 328 (2023), 122509.

[12] M. Zhang, G. Li, Q. Li, J. Chen, E.A. Elimian, H. Jia, H. He, In situ construction of manganese oxide photothermocatalysts for the deep removal of toluene by highly utilizing sunlight energy, Environ. Sci. Technol. 57 (2023) 4286–4297.

[13] T. Xiong, Y. Zhang, W.S.V. Lee, J. Xue, Defect engineering in manganese-based oxides for aqueous rechargeable zinc-ion batteries: a review, Adv. Energy Mater. 10 (2020), 2001769.

[14] T. He, Y. Zhou, D. Ding, S. Rong, Engineering manganese defects in Mn$_3$O$_4$ for catalytic oxidation of carcinogenic formaldehyde, ACS Appl. Mater. Interfaces 13 (2021) 29664–29675.

[15] J. Li, M. Zhang, E.A. Elimian, X. Lv, J. Chen, H. Jia, Convergent ambient sunlight-powered multifunctional catalysis for toluene abatement over in situ exsolution of Mn$_3$O$_4$ on perovskite parent, Chem. Eng. J. 412 (2021), 128560.

[16] Y. Wu, X. Song, S. Li, J. Zhang, X. Yang, P. Shen, L. Gao, R. Wei, J. Zhang, G. Xiao, 3D-monoclinic M–BTC MOF (M = Mn, Co, Ni) as highly efficient catalysts for chemical fixation of CO$_2$ into cyclic carbonates, J. Ind. Eng. Chem. 58 (2018) 296–303.

[17] B. Chen, X. Yang, X. Zeng, Z. Huang, J. Xiao, J. Wang, G. Zhan, Multicomponent metal oxides derived from Mn-BTC anchoring with metal acetylacetonate complexes as excellent catalysts for VOCs and CO oxidation, Chem. Eng. J. 397 (2020), 125424.

[18] G. Zou, H. Hou, X. Cao, P. Ge, G. Zhao, D. Yin, X. Ji, 3D hollow porous carbon microspheres derived from Mn-MOFs and their electrochemical behavior for sodium storage, J. Mater. Chem. A 5 (2017) 23550–23558.

[19] L. Fan, K. Wang, K. Xu, Z. Liang, H. Wang, S.F. Zhou, G. Zhan, Structural isomerism of two Ce-BTC for fabricating Pt/CeO$_2$ nanorods toward low-temperature CO oxidation, Small 16 (2020), e2003597.

[20] M. Mao, Y. Li, J. Hou, M. Zeng, X. Zhao, Extremely efficient full solar spectrum light driven thermocatalytic activity for the oxidation of VOCs on OMS-2 nanorod catalyst, Appl. Catal. B 174–175 (2015) 496–503.

[21] J.-J. Li, E.-Q. Yu, S.-C. Cai, X. Chen, J. Chen, H.-P. Jia, Y.-J. Xu, Noble metal free, CeO$_2$/LaMnO$_3$ hybrid achieving efficient photo-thermal catalytic decomposition of volatile organic compounds under IR light, Appl. Catal. B 240 (2019) 141–152.

[22] Y.-C. Zhang, S. Ullah, R. Zhang, L. Pan, X. Zhang, J.-J. Zou, Manipulating electronic delocalization of Mn$_3$O$_4$ by manganese defects for oxygen reduction reaction, Appl. Catal. B 277 (2020), 119247.

[23] J. Chen, B. Bai, J. Lei, P. Wang, S. Wang, J. Li, Mn$_3$O$_4$ derived from Mn-MOFs with hydroxyl group ligands for efficient toluene catalytic oxidation, Chem. Eng. Sci. 263 (2022) 118065.

[24] Y. Dai, Y. Men, J. Wang, S. Liu, S. Li, Y. Li, K. Wang, Z. Li, Tailoring the morphology and crystal facet of Mn$_3$O$_4$ for highly efficient catalytic combustion of ethanol, Colloid Surf. A 627 (2021), 127216.

[25] B. Zhang, Y. Shen, B. Liu, J. Ji, W. Dai, P. Huang, D. Zhang, G. Li, R. Xie, H. Huang, Boosting ozone catalytic oxidation of toluene at room temperature by using hydroxyl-mediated MnO$_x$/Al$_2$O$_3$ Catalysts, Environ. Sci. Technol. 57 (2023) 7041–7050.

[26] J. Zhao, C. Li, Q. Yu, Y. Zhu, X. Liu, S. Li, C. Liang, Y. Zhang, L. Huang, K. Yang, Z. Zhang, Y. Zhai, Interface engineering of Mn$_3$O$_4$/Co$_3$O$_4$ S-scheme heterojunctions to enhance the photothermal catalytic degradation of toluene, J. Hazard. Mater. 452 (2023), 131249.

[27] H. Jiang, Z. Wei, L. Ma, Y. Yuan, J.J. Hong, X. Wu, D.P. Leonard, J. Holoubek, J. J. Razink, W.F. Stickle, F. Du, T. Wu, J. Lu, X. Ji, An aqueous dual-ion battery cathode of Mn$_3$O$_4$ via reversible insertion of nitrate, Angew. Chem. Int. Ed. 58 (2019) 5286–5291.

[28] Z. Liu, M. Wang, S. Liu, Z. Chen, L. Yang, K. Sun, Y. Chen, L. Zeng, W. Wang, J. Zhao, G. Sun, B. Liu, Y. Pan, Y. Liu, C. Liu, Design of assembled composite of Mn$_3$O$_4$@Graphitic carbon porous nano-dandelions: a catalyst for Low–temperature selective catalytic reduction of NO$_x$ with remarkable SO$_2$ resistance, Appl. Catal. B 269 (2020), 118731.

[29] Y. Lu, H. Deng, T. Pan, X. Liao, C. Zhang, H. He, Effective TOluene Ozonation over δ-MnO$_2$: oxygen vacancy-induced reactive oxygen species, Environ. Sci. Technol. 57 (2023) 2918–2927.

[30] S. Mo, Q. Zhang, J. Li, Y. Sun, Q. Ren, S. Zou, Q. Zhang, J. Lu, M. Fu, D. Mo, J. Wu, H. Huang, D. Ye, Highly efficient mesoporous MnO$_2$ catalysts for the total toluene oxidation: oxygen-vacancy defect engineering and involved intermediates using in situ DRIFTS, Appl. Catal. B 264 (2020), 118464.

[31] J. Gao, Z. Shen, Y. Dong, Z. Wang, J. Lyu, J. Li, H.-Q. Yu, Synergistic effects of Au and PdO$_x$ on the solar-assisted catalytic ozonation of VOCs, J. Mater. Chem. A 11 (2023) 9902–9912.

[32] C. Shan, Y. Zhang, Q. Zhao, K. Fu, Y. Zheng, R. Han, C. Liu, N. Ji, W. Wang, Q. Liu, Acid etching-induced in situ growth of λ-MnO$_2$ over CoMn spinel for low-temperature volatile organic compound oxidation, Environ. Sci. Technol. 56 (2022) 10381–10390.

[33] W. Dai, M. Zou, C. Zhao, J. Zhang, L. Wang, X. Wang, L. Yang, L. Zhou, J. Zou, X. Luo, S. Luo, G. Jing, Monoatomic oxygen fueled by oxygen vacancies governs the photothermocatalytic deep oxidation of toluene on Na-doped Co$_3$O$_4$, Appl. Catal. B 317 (2022), 121769.

[34] J. Li, S. Mo, X. Ding, L. Huang, X. Zhou, Y. Fan, Y. Zhang, M. Fu, Q. Xie, D. Ye, Hollow cavity engineering of MOFs-derived hierarchical MnO$_x$ structure for highly efficient photothermal degradation of ethyl acetate under light irradiation, Chem. Eng. J. 464 (2023), 142412.

[35] N. Ma, Y. Zhang, Y. Wang, C. Huang, J. Zhao, B. Liang, J. Fan, Machine learning-assisted exploration of the intrinsic factors affecting the catalytic activity of ORR/ OER bifunctional catalysts, Appl. Surf. Sci. 628 (2023), 157225.

[36] Y.-C. Zhang, S. Ullah, R. Zhang, L. Pan, X. Zhang, J.-J. Zou, Manipulating electronic delocalization of Mn$_3$O$_4$ by manganese defects for oxygen reduction reaction, Appl. Catal. B 277 (2020), 119247.

[37] S. Zhou, L. Jiang, H. Wang, J. Yang, X. Yuan, H. Wang, J. Liang, X. Li, H. Li, Y. Bu, Oxygen vacancies modified TiO$_2$/O-terminated Ti$_3$C$_2$ composites: unravelling the dual effects between oxygen vacancy and high-work-function titanium carbide, Adv. Funct. Mater. (2023), 2307702.

[38] R. Su, M. He, N. Li, D. Ma, W. Zhou, B. Gao, Q. Yue, Q. Li, Visible-light photocatalytic chlorite activation mediated by oxygen vacancy abundant Nd-doped BiVO$_4$ for efficient chlorine dioxide generation and pollutant degradation, ACS Appl. Mater. Interfaces 14 (2022) 31920–31932.

[39] T.K. Phung, A.A. Casazza, B. Aliakbarian, E. Finocchio, P. Perego, G. Busca, Catalytic conversion of ethyl acetate and acetic acid on alumina as models of vegetable oils conversion to biofuels, Chem. Eng. J. 215–216 (2013) 838–848.

[40] Y. Qin, X. Liu, T. Zhu, T. Zhu, Catalytic oxidation of ethyl acetate over silver catalysts supported on CeO$_2$ with different morphologies, Mater. Chem. Phys. 229 (2019) 32–38.

[41] L. Zhang, Y. Yang, Y. Li, J. Wu, S. Wu, X. Tan, Q. Hu, Highly efficient UV–visible-infrared photothermocatalytic removal of ethyl acetate over a nanocomposite of CeO$_2$ and Ce-doped manganese oxide, Chin. J. Catal. 43 (2022) 379–390.

[42] P.K. Huttunen, D. Labadini, S.S. Hafiz, S. Gokalp, E.P. Wolff, S.M. Martell, M. Foster, DRIFTS investigation of methanol oxidation on CeO$_2$ nanoparticles, Appl. Surf. Sci. 554 (2021), 149518.

[43] Y. Yang, Y. Li, Q. Zhang, M. Zeng, S. Wu, L. Lan, X. Zhao, Novel photoactivation and solar-light-driven thermocatalysis on ε-MnO$_2$ nanosheets lead to highly efficient catalytic abatement of ethyl acetate without acetaldehyde as unfavorable by-product, J. Mater. Chem. A 6 (2018) 14195–14206.

[44] M. Ma, R. Yang, Z. Jiang, C. Chen, Q. Liu, R. Albilali, C. He, Fabricating M/Al$_2$O$_3$/ cordierite (M = Cr, Mn, Fe, Co, Ni and Cu) monolithic catalysts for ethyl acetate efficient oxidation: unveiling the role of water vapor and reaction mechanism, Fuel 303 (2021), 121244.

[45] N. Dong, M. Chen, Q. Ye, D. Zhang, H. Dai, An investigation on catalytic performance and reaction mechanisms of Fe/OMS-2 for the oxidation of carbon monoxide, ethyl acetate, and toluene, J. Environ. Sci. 112 (2022) 258–268.

[46] X. Zhu, S. Zhang, Y. Yang, C. Zheng, J. Zhou, X. Gao, X. Tu, Enhanced performance for plasma-catalytic oxidation of ethyl acetate over La$_{1−x}$Ce$_x$CoO$_{3+δ}$ catalysts, Appl. Catal. B 213 (2017) 97–105.